Unravelling Kinetics of Intramolecular $Nd^{III} \rightarrow Fe^{II}$ Energy Transfer in Spin Crossover Single Molecules: Dotting the *i*'s and Crossing the *t*'s

Deorukhkar, Neel; Glaus, Charlotte; Rosspeintner, Arnulf; Piguet, Claude

How to cite

DEORUKHKAR, Neel et al. Unravelling Kinetics of Intramolecular $Nd^{III} \rightarrow Fe^{II}$ Energy Transfer in Spin Crossover Single Molecules: Dotting the *i*'s and Crossing the *t*'s. In: Journal of the American Chemical Society, 2024, vol. 146, n° 28, p. 19386–19396. doi: 10.1021/jacs.4c05546

This publication URL: https://archive-ouverte.unige.ch/unige:178897
Publication DOI: 10.1021/jacs.4c05546

Publication: *J. Am. Chem. Soc.* **2024**, *146*, 19386-19396. DOI 10.1021/jacs.4c05546

Unravelling Kinetics of Intramolecular $Nd^{III}\rightarrow Fe^{II}$ Energy Transfer in Spin-Crossover Single Molecules: Dotting the i's and Crossing the t's.

Neel Deorukhkar[a], Charlotte Egger[a], Arnulf Rosspeintner[b] and Claude Piguet[a,*]

[a] *Department of Inorganic and Analytical Chemistry. University of Geneva, 30 quai E. Ansermet CH-1211 Geneva 4, Switzerland*

[b] *Department of Physical Chemistry. University of Geneva, 30 quai E. Ansermet CH-1211 Geneva 4, Switzerland*

[*]Email: Claude.Piguet@unige.ch

ABSTRACT: Compared with the ripple of visible Eu^{III}-based emission intensity induced by appended $[Fe^{II}N_6]$ spin crossover (SCO) units, as detected in the triple-stranded $[EuFe(\mathbf{L1})_3]^{5+}$ helicate, the lanthanide-based luminescent detection of Fe^{II} spin-state equilibria could be improved significantly if the luminophore emission is shifted toward the near-infrared (NIR) domain. Replacing Eu^{III} with Nd^{III} in $[NdFe(\mathbf{L1})_3]^{5+}$ (i) maintains the favorable SCO properties in acetonitrile (critical temperature $T_{1/2}$ = 322(2) K), (ii) saturates non-radiative vibrational relaxation processes in the 233-333 K range and (iii) boosts the crucial intramolecular $Nd^{III}\rightarrow Fe^{II}$ energy transfer rate processes which are sensitive to the spin state of the Fe^{II} metallic center. Consequently, the steady-state near-infrared (NIR) $Nd(^4F_{3/2}\rightarrow {}^4I_J)$ emission of the luminophore is amplified and linearly correlated with the LS-$[Fe^{II}N_6]$ and HS-$[Fe^{II}N_6]$ mole fraction controlled by the SCO equilibrium. This paves the way for a straightforward and direct NIR luminescent reading/sensing of Fe^{II} spin state in single molecules.

Introduction

Due to the lack of radial nodes in orbitals characterized by n-l = 1, where n and l are principal, and azimuthal quantum numbers respectively, a property referred to as the primogenic effect,[1] the electronic distributions remain compact in 3d and 4f valence shells,[2-4] which limits overlap, covalencies and perturbation by peripheral partners (i.e. donor atoms). In the case of $[Ar]3d^n$

transition metal ions in coordination complexes, the latter effect limits ligand-field stabilization energies to such an extent that they become competitive with spin pairing energies produced by interelectronic repulsions. Consequently, spin state equilibria come to be accessible at reasonable temperature and/or pressure ranges.[5] In this context, the pseudo-octahedral [$Fe^{II}N_6$] unit,[6] with its $3d^6$ electronic configurations, has been exhaustively exploited for designing thermally-induced or pressure-induced spin crossover (SCO) processes because its compact and enthalpically-favored low-spin (LS) diamagnetic ground state ($^1A_1$) can be switched toward its expanded and entropically-favored high-spin (HS) paramagnetic form ($^5T_2$) in solution[7-10] or in solid materials (eq 1 with $\Delta H_{SCO} > 0$ and $\Delta S_{SCO} > 0$).[11-13]

$$\text{LS-}[Fe^{II}N_6] \quad \underset{k_{HL}}{\overset{k_{LH}}{\rightleftharpoons}} \quad \text{HS-}[Fe^{II}N_6] \qquad K_{SCO} = \frac{k_{LH}}{k_{HL}} = e^{-\Delta G^0_{SCO}/RT} \qquad (1)$$

The associated magnetic modulation, which accompanies the spin transition, is completed by changes in the absorption spectrum of the [$Fe^{II}N_6$] chromophore due to the existence of specific excited levels in the different spin states. The resulting color change can be directly exploited for microscopic thermometry,[14] but the changes of the absorption cross sections [$Fe^{II}N_6$] (in term of both energies and intensities) induced by the low-spin to high-spin transition appear to be more attractive for the implementation of multifunctional magneto-optical response when the emission of an appended polyaromatic luminophore can be controlled by the SCO center.[15-18] These coupled properties are promising for the indirect detection of magnetic switching with superior contrast and sensitivity and high spatial and temporal resolution as demonstrated for thermometers,[19,20] gas sensors[21] and photonic switches.[22-24] The excitation transfer within the energy-donor/acceptor pair may follow a trivial radiative energy transfer where the sensitizer (S = luminophore) absorbs energy, emits a photon which is re-absorbed by the acceptor (A = Fe^{II} SCO unit).[14] This mechanism requires a non-zero spectral overlap $\Omega_{S,A}$ for obeying energy conservation, but it does not depend on the donor/acceptor distance, and the lifetime of the sensitizer is not affected.[25] The latter situation is encountered for green Tb^{III} emitters grafted on [$Fe(Htrz)_2(trz)$]BF_4@SiO_2 spin crossover core shell nanoparticles where the S-A

separation may reach a few tens of nanometers (Figure 1a).[26] When the distance d_{DA} between the sensitizer (now acting as the energy donor D) and the energy acceptor (A) decreases, some non-vanishing electric[25,27-29] and/or magnetic[30] multipolar interactions, possibly completed by wavefunction overlap[31,32] occur. The coupling between the two transition multipoles $\left|\left\langle \psi_{DA^*} \left| H \right| \psi_{D^*A} \right\rangle\right|^2 \neq 0$, expressed for a molecular D-A pair in eq 2 (*H* is the interaction Hamiltonian that mediates energy transfer from the excited donor D^* to the ground-state acceptor A) results in a non-radiative D→A energy transfer characterized by a rate constant $W_{D,A}^{intra}$ modeled with the help of the Fermi golden rule while assuming that there is a non-zero spectral overlap between the two partners ensuring resonance conditions ($\Omega_{D,A} \neq 0$ in eq 2).[33,34]

$$W_{D,A}^{intra} = \frac{2\pi}{\hbar}\left|\left\langle \psi_{DA^*} \left| H \right| \psi_{D^*A} \right\rangle\right|^2 \Omega_{D,A} \qquad (2)$$

With this is mind and using SCO-[$Fe^{II}N_6$] chromophore as the energy acceptor, a ripple of intensity of the steady-state luminescence *via* intramolecular resonant energy transfers has been reported recently for an appended Eu^{III} luminophore in the triple-stranded $[EuFe(\mathbf{L1})_3]^{5+}$ complex in solution (Figure 1b).[35]

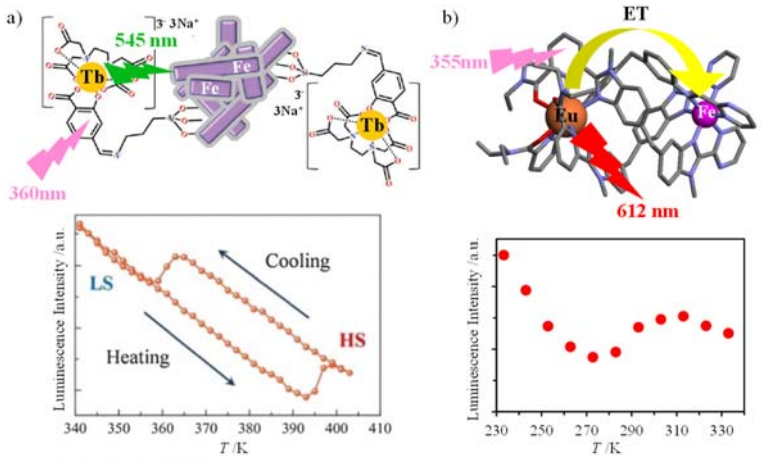

Figure 1. Modulation of steady-state emission intensities of a) Tb^{III} luminophores through Fe^{II}-reabsorption mechanism in $[Fe(Htrz)_2(trz)]BF_4@SiO_2$-$Tb^{III}$ composite (reproduced with permission from reference 26, order License ID 1457099-1, Copyright 2015, Royal Society of Chemistry), and b) Eu^{III} luminophores through intra-molecular resonant energy transfer (ET) mechanism in discrete triple-helical $[EuFe(\mathbf{L1})_3]^{5+}$ complexes.[35]

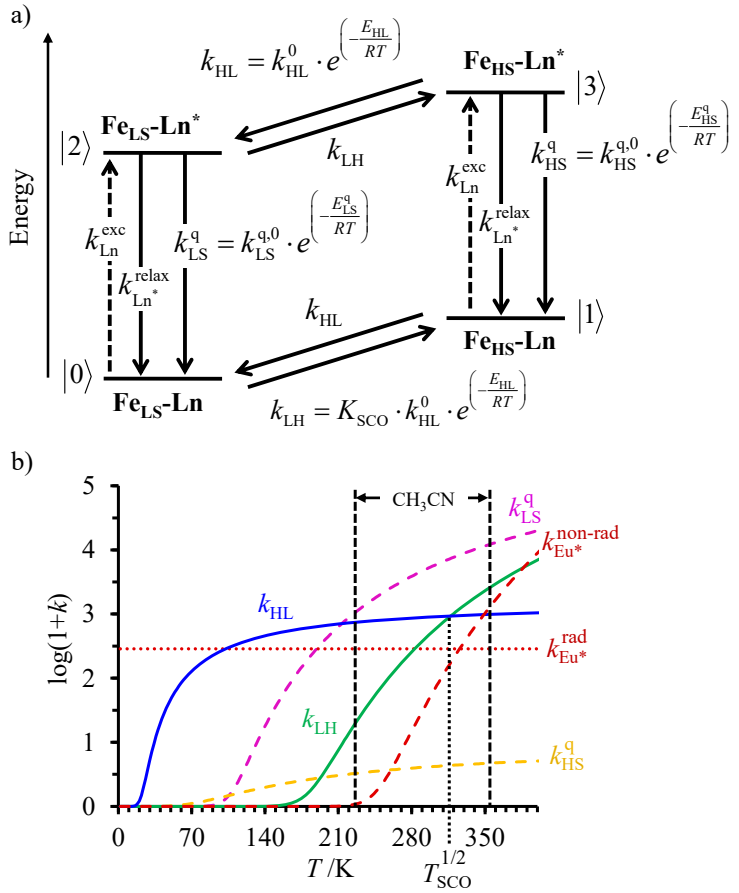

Figure 2 a) Kinetic scheme with dashed upward arrows = excitation, full downward arrows = relaxation and straight diagonal arrows = low-spin ↔ high-spin transformations and b) associated rate constants for the luminescent monitoring of the Fe^{II} spin-state using $Ln^{III} = Eu^{III}$ as luminophore in the dinuclear $[EuFe(\mathbf{L1})_3]^{5+}$ complex ($k^{relax}_{Eu^*} = k^{rad}_{Eu^*} + k^{non\text{-}rad}_{Eu^*}$).[35]

When combined with SCO-Fe^{II} centers, the programing of the line-like emission spectrum of the open-shell trivalent lanthanide partner, Ln^{III},[36-39] can be further exploited for modulating the spectral overlap with the two different spin states.[40] A simple kinetic model pertinent to any coupled SCO-Fe^{II}:Ln^{III} pair (Figure 2a) provides some rational predictions for the steady state ($I^{Ln^*}_{S\text{-}S}$, eq 3) and time-dependent ($I_{Ln^*}(t)$, eq 4) lanthanide-based luminescence intensities (see Appendix 1 for mathematical derivations, $k_A = k_{LH} + k^{relax}_{Ln^*} + k^{q}_{LS}$ and $k_B = k_{HL} + k^{relax}_{Ln^*} + k^{q}_{HS}$).[40]

$$I^{Ln^*}_{S\text{-}S} = k^{rad}_{Ln^*}\left(N^{|2\rangle}_{S\text{-}S} + N^{|3\rangle}_{S\text{-}S}\right) = N_0 k^{exc}_{Ln} k^{rad}_{Ln^*}\left(\frac{k_{LH}\left(k_A + k_{HL}\right) + k_{HL}\left(k_B + k_{LH}\right)}{\left(k_{HL} + k_{LH}\right)\left(k_A k_B - k_{HL} k_{LH}\right)}\right) \quad (3)$$

$$I_{\mathrm{Ln}^*}(t) = k_{\mathrm{Ln}^*}^{\mathrm{rad}}\left(N^{|2\rangle} + N^{|3\rangle}\right) = k_{\mathrm{Ln}^*}^{\mathrm{rad}}\left(\left(C_1 + D_1\right)e^{-k_1 t} + \left(C_2 + D_2\right)e^{-k_2 t}\right) \quad (4)$$

Application of eq 3 to the temperature-dependent steady-state emitted intensity recorded for $[EuFe(\mathbf{L1})_3]^{5+}$ (Figure 1b) gives the kinetic rate constants gathered in Figure 2b (Arrhenius plots collected in Figure S1a).[35] Beyond the unfavorable non-radiative vibrational relaxation $k_{\mathrm{Eu}^*}^{\text{non-rad}}$, which is thermally activated in the 233-333 K range accessible in acetonitrile (see the dashed red trace in Figure 2b), the Eu^{III}-based luminescence is mainly discriminated by the different quenching rate contants $k_{\mathrm{LS}}^{\mathrm{q}}$ (magenta dashed trace in Figure 2b) and $k_{\mathrm{HS}}^{\mathrm{q}}$ (orange dashed trace in Figure 2b) associated with the $Eu^{III}\rightarrow$LS-Fe^{II}, and $Eu^{III}\rightarrow$HS-Fe^{II} energy transfer processes, respectively. Generally speaking, the latter energy transfer processes can be reasonably modeled in $[LnFe(\mathbf{L1})_3]^{5+}$ by focusing on through-space electric dipole/dipole interactions[25,27] according to eq 5,[15,28,29] where κ^2 is an orientation factor, N_A is the Avogadro constant in mmol^{-1}, η is the refractive index of the medium, $k_{\mathrm{D}^*}^{\mathrm{rad}}$ is the radiative rate constant of the donor and J_F is the normalized Förster spectral overlap integral in the wavenumber scale.[41] The dependence of $W_{D,A}$ on temperature, as illustrated for $k_{\mathrm{LS}}^{\mathrm{q}}$ and $k_{\mathrm{HS}}^{\mathrm{q}}$ in Figure 2b, arises from changes in (i) the refractive index, (ii) the radiative rate constants and (iii) the spectral overlap integral.

$$W_{\mathrm{D,A}} = \frac{9\ln(10)\kappa^2 k_{\mathrm{D}^*}^{\mathrm{rad}}}{128\pi^5 N_{\mathrm{A}} n^4 d_{\mathrm{DA}}^6}\cdot J_{\mathrm{F}} \text{ with } J_{\mathrm{F}} = \frac{\int_0^\infty I_{\mathrm{D}^*}^{\bar{\nu}}\varepsilon(\bar{\nu})\left(d\bar{\nu}/\bar{\nu}^4\right)}{\int_0^\infty I_{\mathrm{D}^*}^{\bar{\nu}} d\bar{\nu}} \quad (5)$$

One immediately notices that $W_{D,A}$ is maximum, and thus pertinent to the efficient and versatile tuning of the residual emission a Ln^{III} sensitizer acting as an energy donor, for Ln:Fe pairs possessing (i) a large lanthanide radiative rate constant ($W_{\mathrm{D,A}} \propto k_{\mathrm{D}^*}^{\mathrm{rad}}$), (ii) a short Ln^{III}-Fe^{II} separation ($W_{\mathrm{D,A}} \propto d_{\mathrm{AB}}^{-6}$) and (iii) a considerable spectral overlap integral ($W_{\mathrm{D,A}} \propto J_{\mathrm{F}}$) at low energy ($J_{\mathrm{F}} \propto \bar{\nu}^{-4}$). With this in mind, replacing Eu^{III} with Nd^{III} in $[NdFe(\mathbf{L1})_3]^{5+}$ seems attractive because (i) the visible Eu($^5D_0\rightarrow{}^7F_J$) multiple emission centered at $\bar{\nu}$ = 16340 cm^{-1} (J = 2) is replaced by the lower energy near-infrared (NIR) Nd($^4F_{3/2}\rightarrow{}^4L_J$) emission centered at $\bar{\nu}$ = 9400 cm^{-1} (J = 11/2), (ii) the radiative constant of the

donor $k_{Nd^*}^{rad}$ is increased by one order of magnitude for these spin-allowed Nd^{III} transitions,[42-44] (iv) the low-energy spectral overlap between the Nd-based emission spectrum and the absorption spectrum of HS-[$Fe^{II}N_6$]($^5E \leftarrow {}^5T_2$) at $\bar{\nu}$ =10000 cm^{-1} is largely improved,[45] (v) the thermally-activated vibrational quenching $k_{Nd^*}^{non\text{-}rad}$ is saturated and essentially invariant within the temperature domain accessible in acetonitrile solution[46-48] and, last but not least, (vi) detecting luminescence modulation in the NIR window is highly desirable if efficient and selective time-gated detection has to be implemented in complicated hybrid materials or media.[12,15,49]

Results and Discussion

Synthesis and molecular structures of the self-assembled triple-stranded helicates $[NdM(L1)_3]^{5+}$ (M = Fe, Zn). As previously established for the complete $[LnM(\mathbf{L1})_3]^{5+}$ series (Ln = La, Nd, Eu and M = Zn, Fe),[35] stoichiometric reactions of 3 eq. of ligand **L1** with 1 eq. of $Zn(CF_3SO_3)_2$ or $Fe(CF_3SO_3)_2$ and 1 eq. $Nd(CF_3SO_3)_3$ in acetonitrile yielded microcrystalline powders of complexes $[NdM(\mathbf{L1})_3](CF_3SO_3)_5$. The powders, when re-dissolved in acetonitrile and allowed to crystallize by (very) slow diffusion of diethyl ether yielded single crystals of $[NdZn(\mathbf{L1})_3](CF_3SO_3)_5 \cdot 1.5CH_3CN$ and $[NdFe(\mathbf{L1})_3](CF_3SO_3)_5 \cdot 2CH_3CN \cdot 0.5C_4H_{10}O$ which could be characterized by X-ray diffraction at 120 K (Figure 3).[35] The molecular structures of $[NdM(\mathbf{L1})_3]^{5+}$ (M= Fe, Zn) cations display the three ligand strands of **L1** wrapped about the two cations separated by a distance of circa 9 Å. The head-to-head-to-head arrangement of the three strands leading to the C_3-symmetric triple-helical structure is confirmed in solution by the detection of a single set of aromatic protons for the ligand **L1** (threefold axis), together with appearance of [AB] spin systems for diastereotopic methylene protons in (i) the interaromatic bridges (protons l) and (ii) the terminal amide groups (protons b and c) (Figure S2). Interestingly, Nd^{3+} ([Xe]$4f^3$) and Eu^{3+} ([Xe]$4f^6$) possess opposite spin expectation values ($\langle S_z \rangle$ -4.49 *versus* 10.68) and opposite Bleaney factors (C = -4.2 *versus* 4.0).[50] For these isostructural $[LnZn(\mathbf{L1})_3]^{5+}$ (Ln = Nd, Eu) complexes, this trend results in reversed (but with similar magnitude) lanthanide-induced paramagnetic shifts when $[NdZn(\mathbf{L1})_3]^{5+}$ (Figure S2), and

$[EuZn(\mathbf{L1})_3]^{5+}$ (Figure S3) are compared with respect to the diamagnetic $[LaZn(\mathbf{L1})_3]^{5+}$ taken as a reference. The antagonistic chemical shifts of the pyridine protons (e, f and g; green traces in Figures S2-S3) demonstrate opposite through-bond contact effects via $\langle S_z \rangle$. The adverse shifts of the protons located close to the paramagnetic lanthanide within the helix (c, d, o and k; red traces in Figures S2-S3) highlight reverse pseudo-dipolar shifts controlled by Bleaney factors *C* in complete agreement with a simple exchange of Nd^{3+} with Eu^{3+} without affecting the triple-helical structure in solution.[51]

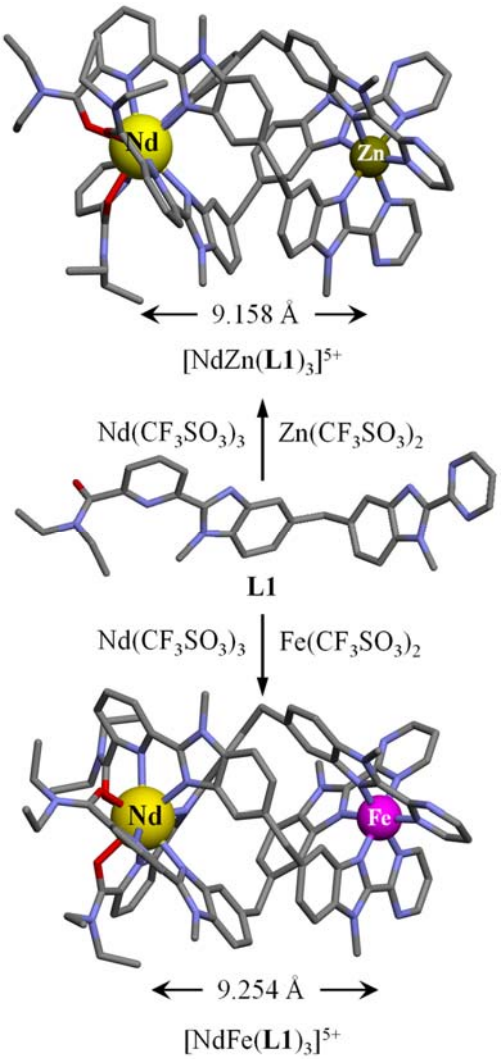

Figure 3. Molecular structures of the ligand **L1** (CCDC 2287440) and the cationic triple-stranded helicates $[NdZn(\mathbf{L1})_3]^{5+}$ and $[NdFe(\mathbf{L1})_3]^{5+}$ as observed in the crystal structures of **L1** (CCDC 2287440), $[NdZn(\mathbf{L1})_3](CF_3SO_3)_5 \cdot 1.5CH_3CN$ (CCDC 2287442) and $[NdFe(\mathbf{L1})_3](CF_3SO_3)_5 \cdot 2CH_3CN \cdot 0.5C_4H_{10}O$ (CCDC 2287445).[35]

[NdZn(L1)$_3$]$^{5+}$ as a model for extracting radiative and non-radiative Nd-centered relaxation decay rate constants in solution. Beyond the intense spin- and parity-allowed ligand-centered $^1\pi^* \leftrightarrow {}^1\pi$ transitions covering the UV-to-blue part (200-400 nm) of the absorption/emission spectra of the [LnZn(**L1**)$_3$]$^{5+}$ complexes in solution (Figures S4), the choice of the lanthanide determines the metal-based parity-forbidden line-like 4f-4f absorption/emission bands covering the visible-to-NIR spectral domain (Figures 4 and S4c). Due to non-negligible spin-orbit coupling, the spin conservation rule is partially relaxed for the metal-based transitions whereas pseudo-quadripolar obeying $\Delta J = \pm 2$ and $\Delta L = \pm 2$ may become hypersensitive depending on the coordination spheres.[40-42]

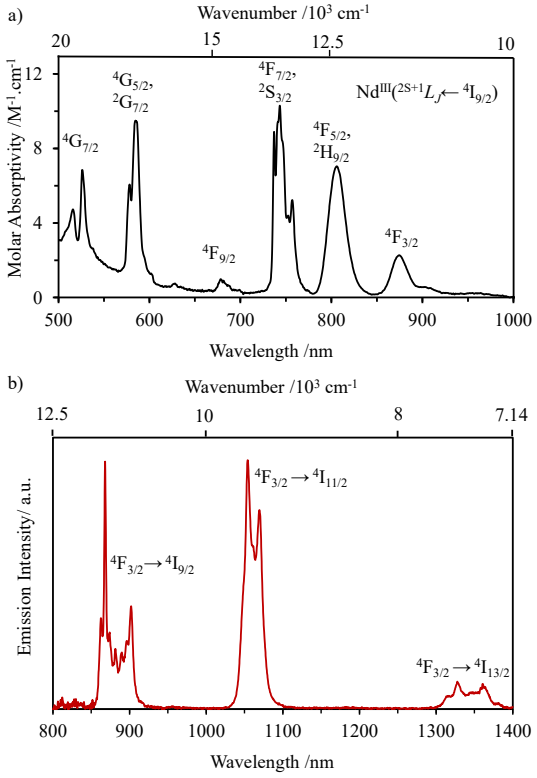

Figure 4. Electronic a) absorption and b) emission spectra (λ_{exc} = 331 nm, long-pass 515 nm filter at emission) of a 0.998 mM solution of [NdZn(**L1**)$_3$]$^{5+}$ in acetonitrile at 293 K showing Nd($^{2S+1}L_J \leftarrow {}^4I_{9/2}$) absorption transitions and Nd($^4F_{3/2} \rightarrow {}^4I_J$) emission transitions.

The Jabłoński diagram previously established for [EuZn(**L1**)$_3$]$^{5+}$ (left part of Figure 5)[35] can be easily extended for [NdZn(**L1**)$_3$]$^{5+}$ (right part of Figure 5) where the antenna effect, beyond some residual

$^1\pi_2^* \rightarrow {}^1\pi$ fluorescence (Figure S4a), induces Nd-centered luminescence arising from the spin-allowed Nd($^4F_{3/2} \rightarrow {}^4I_J$) transitions ($J$ = 13/2, 11/2 and 9/2 ; Figure 4b).

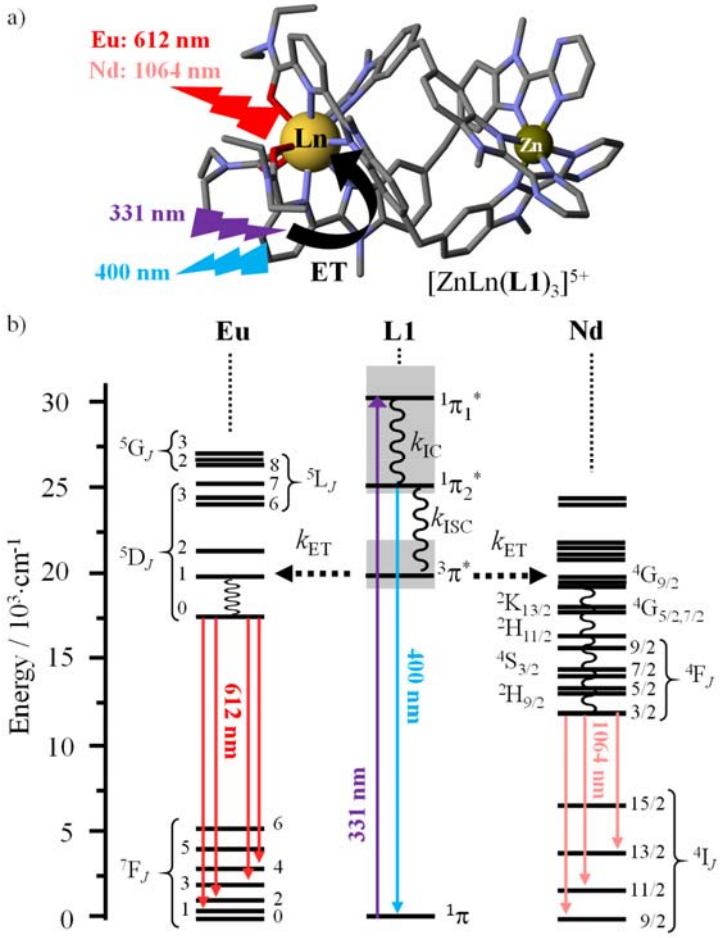

Figure 5. Jabłoński diagram summarizing the excitation processes (straight upward magenta arrow), energy transfers (dashed arrows), non-radiative multi-phonon relaxation (undulating arrows) and radiative emission processes (straight downward arrows) operating in $[LnZn(\mathbf{L1})_3]^{5+}$ (Ln = Nd, Eu). Only the ligand-to-metal energy transfers arising from triplet states are shown. The labels of Ln-centered excited states are taken from ref 60.

The radiative rate constant $k_{Nd^*}^{rad}\left({}^4F_{3/2} \leftrightarrow {}^4I_{9/2}\right)$ = 1145(52) s^{-1} of the specific Nd($^4F_{3/2} \leftrightarrow {}^4I_{9/2}$) transition ($\lambda \sim$ 868 nm), which connects the $^4I_{9/2}$ ground level with the unique emissive $^4F_{3/2}$ excited state, is easily deduced from the absorption spectrum (Figure 4a) by using the Strickler-Berg eq A2-1 (Appendix 2).[52-54] The complementary radiative processes, responsible for the total decay of the

emissive Nd($^4F_{3/2}$) are estimated with $k^{rad}_{Nd^*,i} = \left(\beta_i / \beta_{ref}\right) k^{rad}_{Nd^*,ref}$ where $\beta_i = I^{em}_i / I^{em}_{tot}$ is the branching ratio[55] of the emissive transition i (I^{em} are the integrated intensities of $^4F_{3/2} \rightarrow {}^4I_J$ emission bands, while reasonably assuming that the $^4F_{3/2} \rightarrow {}^4I_{15/2}$ transition at $\lambda > 1700$ nm contributes negligibly to the radiative decay ($\beta_4 = 0$), Appendix 2).[56] The estimated radiative rate constants $k^{rad}_{Nd^*}\left({}^4F_{3/2} \leftrightarrow {}^4I_{11/2}\right)$ = 1817(88) s^{-1} at $\lambda \sim 1056$ nm and $k^{rad}_{Nd^*}\left({}^4F_{3/2} \leftrightarrow {}^4I_{13/2}\right)$ = 375(18) s^{-1} at $\lambda \sim 1332$ nm can be combined with $k^{rad}_{Nd^*}\left({}^4F_{3/2} \leftrightarrow {}^4I_{9/2}\right)$ = 1145(52) s^{-1} to give the total radiative rate constant $k^{rad}_{Nd^*}\left({}^4F_{3/2}\right)$ = 3337(103) s^{-1} (Tables 1 and A2-1). It finally translates into $\tau^{rad}_{Nd^*}\left({}^4F_{3/2}\right)$ = 0.30(1) ms for $[NdZn(\mathbf{L1})_3]^{5+}$ in acetonitrile at 293 K, in good accord with previously reported values for Nd^{III} emitters bound to N-donor ligands.[57,58] Compared to $\tau^{rad}_{Eu^*}\left({}^5D_0\right)$ = 3.50(1) ms reported for $[EuZn(\mathbf{L1})_3]^{5+}$ (i.e. $k^{rad}_{Eu^*}\left({}^5D_0\right)$ = 286(1) s^{-1})[35] the increase of $k^{rad}_{Ln^*}$ by one order of magnitude in $[NdZn(\mathbf{L1})_3]^{5+}$ confirms the partial respect of the spin-rule for 4f-4f electronic transitions operating in light lanthanides. This compensates for the opposite cubic dependence on the energy gap $k^{rad}_{Ln^*} \propto \left(\bar{\nu}\right)^3$,[59] which is indeed reduced from $\bar{\nu}$ = 17240 cm^{-1} for Eu^{III} (red emission) to 11520 cm^{-1} for Nd^{III} (NIR emission).

Reasonably considering a negligible hyperbolic cotangent dependence[61] of the radiative rate constants on the average phonon bath found in lanthanide coordination complexes ($h\nu \approx 2000$ cm^{-1}),[35,62] the decay rate constants of the excited Nd($^4F_{3/2}$) spectroscopic level can be partitioned between a uniform radiative ($k^{rad}_{Nd^*}$), and a thermally-activated non-radiative contribution ($k^{non\text{-}rad}_{Nd^*}$) modeled with an Arrhenius-type phonon-assisted deactivation mechanism summarized in eq 6 ($k^{non\text{-}rad,0}_{Nd^*}$ stands for the non-radiative relaxation at $T \rightarrow \infty$ and $E^{non\text{-}rad}_{Nd}$ is the activation energy of the phonon-assisted relaxation pathway, and the low-temperature tunneling, being much smaller than the radiative decay, is neglected).[40,62,63]

$$k_{\mathrm{Nd}^*}^{\mathrm{relax}} = k_{\mathrm{Nd}^*}^{\mathrm{rad}} + k_{\mathrm{Nd}^*}^{\mathrm{non\text{-}rad},0} \cdot \exp\left(-\frac{E_{\mathrm{non\text{-}rad}}}{RT}\right) \quad (6)$$

Variable temperature emission spectra of $[NdZn(\mathbf{L1})_3]^{5+}$ (λ_{exc} = 331 nm) in acetonitrile show only a marginal decrease in the intensity of $^4F_{3/2} \rightarrow {}^4I_J$ transitions with an increase in temperature (Figure 6a). This trend is confirmed by a minor increase in the total relaxation rate constant ($k_{\mathrm{Nd}^*}^{\mathrm{relax}}$, Figure 6b) measured for the Nd($^4F_{3/2} \rightarrow {}^4I_{11/2}$) transition at 1064 nm under nanosecond pulsed excitation (Nd:YAG, λ_{exc} = 355 nm).

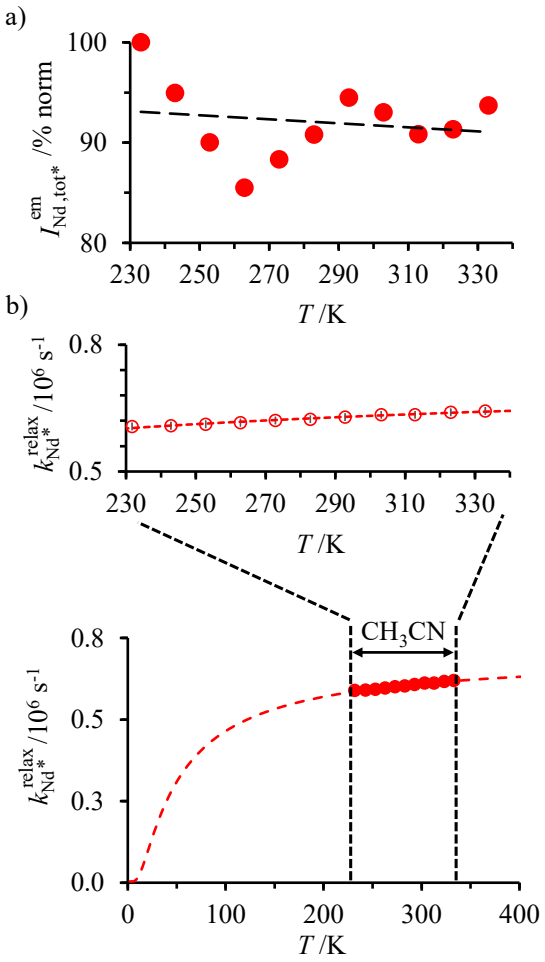

Figure 6. Plots of a) total normalized Nd($^4F_{3/2}$) emission intensity $I^{em}_{Nd^*,tot} / I^{em}_{Nd^*,max} = I_{tot}/I_{233K}$ (the dashed black trace is only a trendline for the eyes) and b) Nd($^4F_{3/2}$) relaxation rate constants $k_{\mathrm{Nd}^*}^{\mathrm{relax}}$ (Nd:YAG, λ_{exc} = 355 nm) as a function of the temperature (T) for $[NdZn(\mathbf{L1})_3]^{5+}$ in acetonitrile solution. The dashed red traces are plotted with eq 6 using the best fit with $k_{rad} = 3.337(103)\cdot10^3$ s^{-1}, $k_{\mathrm{Nd}^*}^{\mathrm{non\text{-}rad},0} = 6.9527(1)\cdot10^5$ s^{-1} and $E_{non\text{-}rad} = 0.34(1)$ kJ·mol^{-1} (Table 1).

The microsecond regime of the observed excited Nd($^4F_{3/2}$) decay lifetime $\tau_{Nd^*}^{obs} = 1/k_{Nd^*}^{relax}$ (Table S1 and Figure 6b) contrasts with the close-to millisecond contribution of the radiative process ($\tau_{Nd^*}^{rad}\left({}^4F_{3/2}\right)$ = 0.30(1) ms). It can be assigned to efficient coupling with ligand vibrations[64] since the energy gap $\Delta E = E(^4F_{3/2})-E(^4I_{15/2}) \approx 5900$ cm^{-1} corresponds to only twice the energy of the aromatic C-H stretching modes.[65] The latter thermally-activated non-radiative process has been fitted using eq 6 to give $k_{Nd^*}^{non\text{-}rad,0} = 6.9527(1)\cdot10^5$ s^{-1} with a very minor activation energy $E_{non\text{-}rad} = 0.34(1)$ kJ·mol^{-1} (Table 1), which is overcome in the 233-333K range accessible in acetonitrile (Figure 6b). Altogether, the efficient vibrational quenching of Nd($^4F_{3/2}$) luminescence is responsible for the low and rather invariant intrinsic quantum yield of [NdZn(**L1**)$_3$]$^{5+}$ in acetonitrile solution ($\Phi_{Nd}^{Nd} = k_{Nd^*}^{rad}/k_{Nd^*}^{relax}$ = 0.00393(1)).

Modulation of Nd-based luminescence upon Fe(II) spin crossover operating in [NdFe(L1)$_3$]$^{5+}$ complex in solution. Introducing a Fe^{II}-chromophore, instead of Zn^{II}, in [NdFe(**L1**)$_3$]$^{5+}$ does not significantly affect the ligand-based or Nd^{III}-based electronic levels, but it brings novel metal-to-ligand charge transfer (MLCT) states together with Fe^{II}-based levels (Figure 7) which are specific to the high-spin (HS-[NdFe(**L1**)$_3$]$^{5+}$) and low-spin (LS-[NdFe(**L1**)$_3$]$^{5+}$) forms.[45] It is worth reminding here that the population of the ground states are thermally controlled by eq 1 with ΔH_{SCO}^0 = 23.1(1) kJ·mol^{-1} and ΔS_{SCO}^0 = 71.8(1) J·mol^{-1}·K^{-1}, which gives a transition temperature $T_{1/2} = \Delta H_{SCO}^0/\Delta S_{SCO}^0$ = 322(2) K for the latter complex.[35] The temperature-dependent absorption spectra of [NdFe(**L1**)$_3$]$^{5+}$ in acetonitrile confirm this analysis with no significant change of the low-energy Nd($^{2S+1}L_J \leftarrow {}^4I_{9/2}$) transitions, but the detection of an intense and variable absorbance in the visible part, which is diagnostic for the spin-allowed MLCT transitions of LS-[NdFe(**L1**)$_3$]$^{5+}$ (Figure 8a and S5a). The observed blue shift of the MLCT bands upon the thermally-induced transformation of LS-[NdFe(**L1**)$_3$]$^{5+}$ into HS-[NdFe(**L1**)$_3$]$^{5+}$ (Figures 8 and S5) was detailed previously for [LaFe(**L1**)$_3$]$^{5+}$ (Figure S6).[35] One also notes the existence of broad and non-negligible absorption bands within the

700-1000 nm domain for both LS/HS-[$Fe^{II}N_6$] chromophores (NIR, Figure 8a), which are lacking for [NdZn(**L1**)$_3$]$^{5+}$ (Figure 4a and Figure S7), but fully compatible with the induction of resonant energy transfer from the Nd($^4F_{3/2}$) level via the Förster mechanism (eq 5) since the spectral overlap between the emission spectrum of the Nd^{III}-donor and the absorption spectrum of the Fe^{II}-acceptor is therefore not negligible in [NdFe(**L1**)$_3$]$^{5+}$ (Figure 8b). For LS-[$Fe^{II}N_6$], the NIR absorption can be tentatively assigned to the low-energy tail of the MLCT transition together with weak spin-forbidden ligand-field LS-Fe(^{3,5}T←^{1}A) electronic transitions (Figure 7). For the C_3-symmetrical HS-[NdFe(**L1**)$_3$]$^{5+}$, the non-negligible intensity of the spin-allowed HS-Fe(^{5}E←^{5}T) transition may explain the reinforced absorption in the NIR at high temperature (Figure 8a).[45]

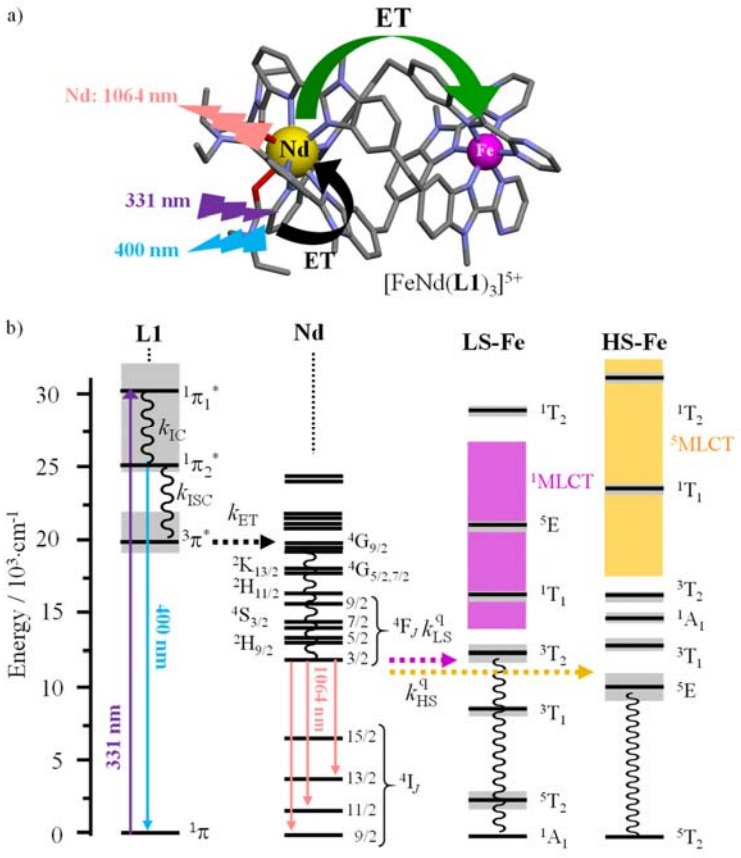

Figure 7. Jabłoński diagram summarizing the excitation processes (straight upward arrows), energy transfers (dashed arrows), non-radiative multi-phonon relaxation (undulating arrows) and radiative emission processes (straight downward arrows) operating in LS-[NdFe(**L1**)$_3$]$^{5+}$ and HS-[NdFe(**L1**)$_3$]$^{5+}$.

As expected, the radiative rate constants $k_{Nd^*}^{rad}\left({}^4F_{3/2} \leftrightarrow {}^4I_{9/2}\right)$ estimated from the integration of the absorption spectra of [NdFe(**L1**)$_3$]$^{5+}$ with eq A2-1 do not depend on temperature and strictly mirror that previously extracted for [NdZn(**L1**)$_3$]$^{5+}$ (Figure A2-3 in Appendix 2).[52-54]

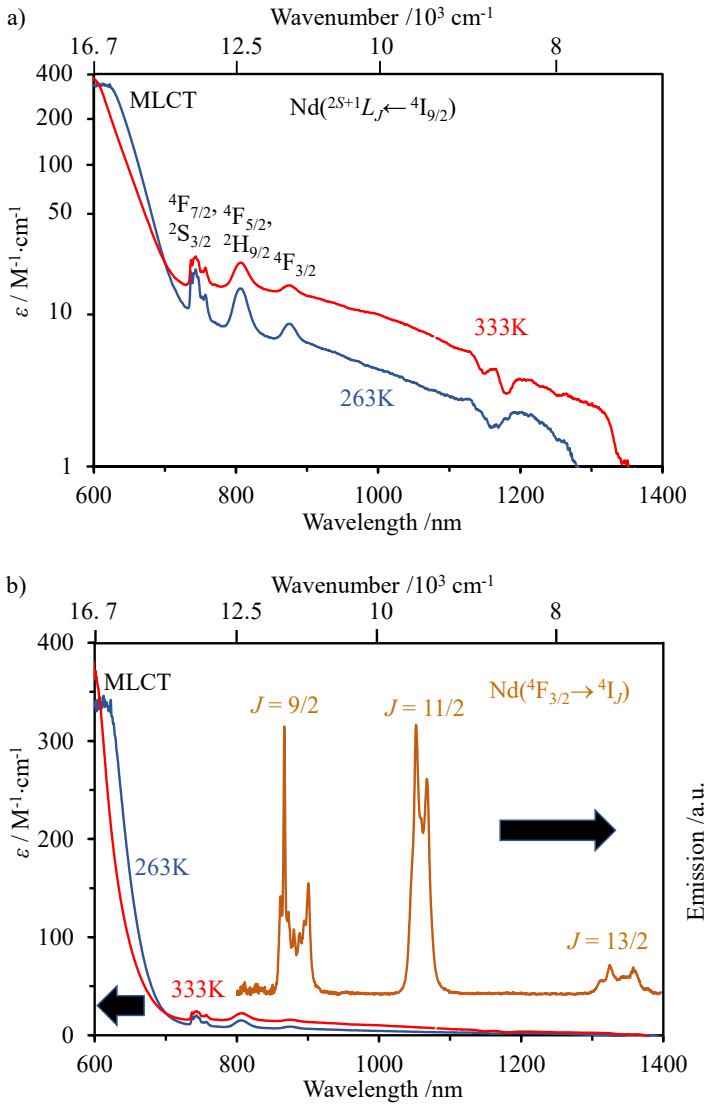

Figure 8. a) Temperature-dependent absorption spectra recorded for [NdFe(**L1**)$_3$]$^{5+}$ in acetonitrile (10 mM) and b) corresponding emission spectrum at 293 K (λ_{exc} = 331 nm).

Besides the radiative ($k_{Nd^*}^{rad}$) and non-radiative ($k_{Nd^*}^{non\text{-}rad}$) relaxation mechanisms affecting the Nd($^4F_{3/2}$) emissive level, which can be reasonably considered as similar for [NdFe(**L1**)$_3$]$^{5+}$ and [NdZn(**L1**)$_3$]$^{5+}$

(eq 6), the two intramolecular energy transfers Nd^{III}→LS-Fe^{II} (k^{q}_{LS}, eq 7) and Nd^{III}→HS-Fe^{II} (k^{q}_{HS}, eq 8) further contribute to quench the lanthanide-based luminescence (Figure 7).[35,40]

$$k^{q}_{LS} = k^{q,0}_{LS} \cdot \exp\left(-\frac{E^{q}_{LS}}{RT}\right) \quad (7)$$

$$k^{q}_{HS} = k^{q,0}_{HS} \cdot \exp\left(-\frac{E^{q}_{HS}}{RT}\right) \quad (8)$$

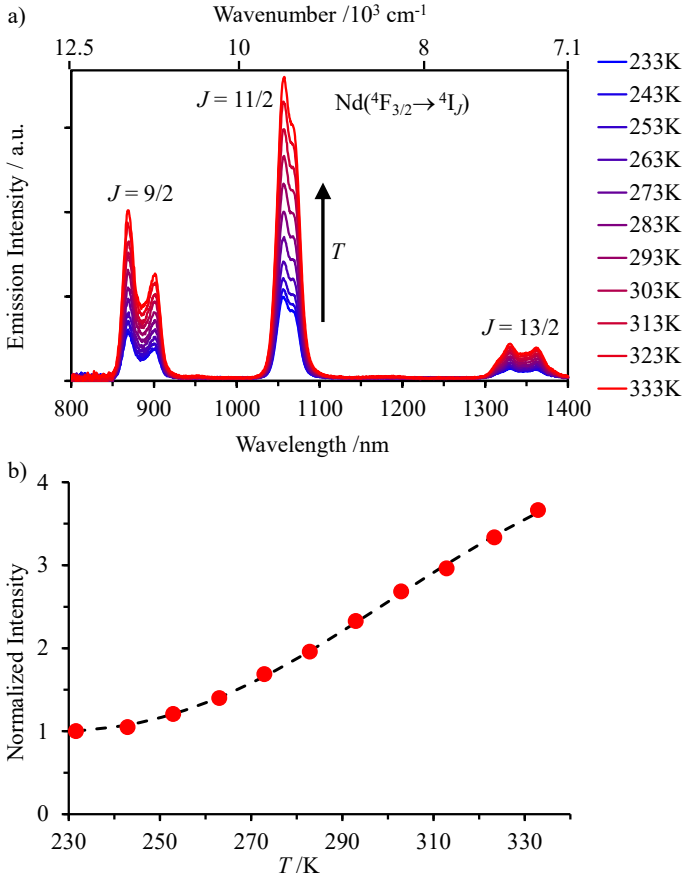

Figure 9. a) Emission spectra of $[NdFe(\mathbf{L1})_3]^{5+}$ in acetonitrile between 233-333 K (λ_{exc} = 331 nm) b) associated plot of normalized total integrated intensity ($I/I_{max} = I_T/I_{233K}$) for emission from Nd^{III} ($^4F_{3/2}$→ ^4I_J) in $[NdFe(\mathbf{L5})_3]^{5+}$ (red circles) vs. temperature (T). The dashed black trace circles represent the non-linear least squares fitted intensities computed with eq 3 and using the values collected in Table 1 column 2 (AF = 0.0001).

Moreover, the complete kinetic mechanism summarized in Figure 2a combines the first-order rate constants for low-spin→high-spin (k_{HL}) and high-spin→low-spin transitions (k_{LH}) with the thermodynamic SCO equilibrium constants in eqs 9-10.[35,40]

$$k_{HL} = k_{HL}^{0} \cdot \exp\left(-\frac{E_{HL}}{RT}\right) \quad (9)$$

$$\frac{k_{LH}}{k_{HL}} = K_{SCO} \Rightarrow k_{LH} = K_{SCO} \cdot k_{HL}^{0} \cdot \exp\left(-\frac{E_{HL}}{RT}\right) \quad (10)$$

Upon weak continuous excitation of $[NdFe(\mathbf{L1})_3]^{5+}$ in acetonitrile at $P \approx 8.1$ mW·cm^{-2} using a Xenon lamp (λ_{exc} = 331 nm), the emission spectra display the standard NIR active Nd^{III}-based transitions (Figure 9a), the total intensity of which unusually smoothly increases with temperature (Figure 9b). In these excitation conditions, the excited state populations ($N_{S\text{-}S}^{|2\rangle}$ and $N_{S\text{-}S}^{|3\rangle}$ in Figure 2a) are negligible with respect to the ground state populations, so that $\frac{N_{S\text{-}S}^{|1\rangle}}{N_{S\text{-}S}^{|0\rangle}} \approx \frac{N_{0}^{|1\rangle}}{N_{0}^{|0\rangle}} = \frac{k_{LH}}{k_{HL}} = K_{SCO} = \exp\left(-\frac{\Delta G_{SCO}^{0}}{RT}\right)$ and $N_{S\text{-}S}^{|0\rangle} + N_{S\text{-}S}^{|1\rangle} = N_0$. The total steady-state emitted intensity $I_{S\text{-}S}^{Nd^*}$ then obeys eq 3 (Appendix 1), which allows some further modeling. In line with the negligible effect of the nature of the selected lanthanide cations on the SCO properties of the $[LnFe(\mathbf{L1})_3]^{5+}$ complexes in solution,[35] the kinetic and thermodynamic constants deduced for $[EuFe(\mathbf{L1})_3]^{5+}$ spin-state equilibrium in solution (eqs 9-10) are considered pertinent for $[NdFe(\mathbf{L1})_3]^{5+}$ (Table 1). Similarly, the radiative and non-radiative Nd^{III}-based relaxation pathways extracted for $[NdZn(\mathbf{L1})_3]^{5+}$ summarized in eq 6 are taken as identical for $[NdFe(\mathbf{L1})_3]^{5+}$ (Table 1). With this in mind, a careful non-linear least-squares fit of the normalized experimental emission intensity in $[NdFe(\mathbf{L1})_3]^{5+}$ (I_T/I_{233K}, plotted as red circles in Figure 9b) with eq 3 provides satisfying reproduction of the experimental measurements (black dashed trace in Figure 9b) while converging to $k_{LS}^{q,0}$ = 2.1801(2)·10^8 s^{-1} and E_{LS}^{q} = 4.9682(5) kJ.mol^{-1} for the intramolecular Nd^{III}→LS-Fe^{II} energy transfer (eq 7) and $k_{HS}^{q,0}$ = 3.626(1)·10^6 s^{-1} and E_{HS}^{q} = 2.4372(3) kJ.mol^{-1} for Nd^{III}→HS-Fe^{II} energy transfer (eq 8, Table 1 column 2). Compared with $[EuFe(\mathbf{L1})_3]^{5+}$, both Fe^{II}-based quenching processes are more efficient in $[NdFe(\mathbf{L1})_3]^{5+}$, which results in gain by three orders of magnitude for the quenching rate constant by LS-Fe^{II} (k_{LS}^{q}) and up to five orders of magnitude for quenching by HS-Fe^{II} (k_{HS}^{q}) in the 233-333 K range (Table 2). Since the Ln···Fe distance is not altered, the origin of this trend can be partitioned with eq 5 between (i) a predicted increase of the $k_{D^*}^{rad}/\bar{\nu}^4$

ratio by two orders of magnitudes when a visible Eu^{III} emitter ($\bar{\nu}_{em} \approx 16300$ cm^{-1}) is replaced with a NIR Nd^{III} emitter ($\bar{\nu}_{em} \approx 10000$ cm^{-1}) and (ii) a complementary increase of the Förster spectral overlap integral J_F. The existence of a specific low-energy spin-allowed d-d transition for HS-[$Fe^{II}N_6$] within the NIR domain covered by the Nd^{III}-emission spectrum might contribute to the notably larger values observed for k_{HS}^{q} upon replacing Eu^{III} with Nd^{III}.[45]

Table 1. Rate constants and activation barriers estimated for various relaxation processes of Ln^{III} shown in Figure 2a and steady-state emission upon continuous excitation (eq 3) for [EuFe(**L1**)$_3$]$^{5+}$ and [NdFe(**L1**)$_3$]$^{5+}$.[a]

	[EuFe(**L1**)$_3$]$^{5+}$	[NdFe(**L1**)$_3$]$^{5+}$
$k_{Ln^*}^{rad}$ /s^{-1}	285.7(4) [b]	3.337(103)·10^3 [c]
$k_{Ln^*}^{non\text{-}rad,0}$ /s^{-1}	3.155(5)·10^{10} [b]	6.9527(1)·10^5 [c]
$E_{non\text{-}rad}$ /kJ·mol^{-1}	50.16(8) [b]	0.34(1) [c]
$k_{HS}^{q,0}$ /s^{-1}	8.850(4)	3.626(1)·10^6
E_{HS}^{q} /kJ·mol^{-1}	2.560(1)	2.4372(3)
$k_{LS}^{q,0}$ /s^{-1}	8.948(5)·10^5	2.1801(2)·10^8
E_{LS}^{q} /kJ.mol^{-1}	12.670(6)	4.9682(5)
k_{HL}^{0} /s^{-1}	1.63192(8)·10^3	1.63192(8)·10^3 [d]
E_{HL} /kJ·mol^{-1}	1.485(1)	1.485(1) [d]
k_{LH}^{0} /s^{-1}	1.53133(8)·10^7	1.53133(8)·10^7 [d]
E_{LH} /kJ·mol^{-1}	25.61(2)	25.61(2) [d]
Reference	35	This work

[a] The quoted uncertainties correspond to those of the fitting processes. The experimental uncertainties are larger and typically within the 2-5% range. [b] Measured for [EuZn(**L1**)$_3$]$^{5+}$. [c] Measured for [NdZn(**L1**)$_3$]$^{5+}$. [d] Values of k_{HL}^{0}, k_{LH}^{0}, E_{HL} and E_{LH} found for [EuFe(**L1**)$_3$]$^{5+}$.

Table 2. Kinetic rate constants associated with the intramolecular d-f energy transfer (k_{LS}^{q}, k_{HS}^{q}), SCO process (k_{HL} and k_{LH}) and non-radiative decay ($k_{Ln^*}^{non\text{-}rad}$) computed at 233, 293, and 333 K for complexes $[EuFe(\mathbf{L1})_3]^{5+}$ [35] and $[NdFe(\mathbf{L1})_3]^{5+}$ based on steady-state measurement (Table 1).[a]

	233 K		293 K		333 K	
	$[EuFe(\mathbf{L1})_3]^{5+}$	$[NdFe(\mathbf{L1})_3]^{5+}$	$[EuFe(\mathbf{L1})_3]^{5+}$	$[NdFe(\mathbf{L1})_3]^{5+}$	$[EuFe(\mathbf{L1})_3]^{5+}$	$[NdFe(\mathbf{L1})_3]^{5+}$
$k_{Ln^*}^{non\text{-}rad}$ /s^{-1} [b]	0.17961(9)	$5.8289(4)\cdot10^5$	36.05(35)	$6.0432(4)\cdot10^5$	427(4)	$6.1458(4)\cdot10^5$
k_{HS}^{q} /s^{-1}	2.361(1)	$1.0306(1)\cdot10^6$	3.09(3)	$1.3335(1)\cdot10^6$	3.511(34)	$1.5037(2)\cdot10^6$
k_{LS}^{q} /s^{-1}	$1.2918(6)\cdot10^3$	$1.6775(2)\cdot10^7$	$4.93(49).10^3$	$2.8363(3)\cdot10^7$	$9.21(9).10^3$	$3.6236(4)\cdot10^7$
k_{HL} /s^{-1} [c]	$7.586(38)\cdot10^2$		$8.872(88)\cdot10^2$		$9.546(92)\cdot10^2$	
k_{LH} /s^{-1} [c]	27.83(1)		$4.169(14)\cdot10^2$		$1.473(14)\cdot10^3$	
$\eta_{Ln\rightarrow Fe_{LS}}^{ET}$ [d]	81.9%	96.6%	93.9%	97.9%	92.8%	98.3%
$\eta_{Ln\rightarrow Fe_{HS}}^{ET}$ [e]	0.8%	63.7%	1.0%	68.7%	0.5%	70.9%

[a] The quoted uncertainties correspond to those of the fitting processes. The experimental uncertainties are larger and typically within the 2-5% range. [b] Measured for $[LnZn(\mathbf{L1})_3]^{5+}$. [c] Calculated for $[EuFe(\mathbf{L1})_3]^{5+}$. [d] $\eta_{Ln\rightarrow Fe_{LS}}^{ET} = \frac{k_{LS}^{q}}{k_{LS}^{q} + k_{Ln^*}^{relax}} \times 100$. [e] $\eta_{Ln\rightarrow Fe_{HS}}^{ET} = \frac{k_{HS}^{q}}{k_{HS}^{q} + k_{Ln^*}^{relax}} \times 100$.

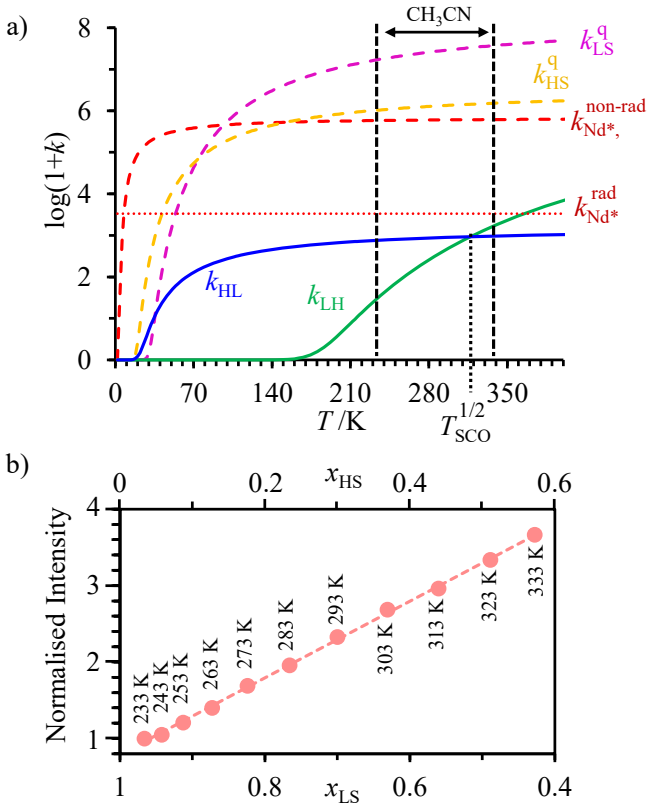

Figure 10 a) Kinetic rate constants (see Figure 2a for the scheme) and b) steady-state Nd($^4F_{3/2}$) NIR emission luminescence monitoring of the Fe^{II} spin-state in the dinuclear $[NdFe(\mathbf{L1})_3]^{5+}$ helicate in acetonitrile (x_{LS} = 1-x_{HS} is the mole fraction of low-spin Fe^{II}).

In line with $[EuFe(\mathbf{L1})_3]^{5+}$, where k_{LS}^{q} was shown to be responsible for 80-90% of the total relaxation of the emissive Eu($^5D_0$) level in acetonitrile (233-333 K range, Figure S8a),[35] the related intramolecular quenching of the emissive Nd($^4F_{3/2}$) level by low-spin Fe^{II} in $[NdFe(\mathbf{L1})_3]^{5+}$ accounts for more than 90% of the global deactivation mechanism in solution (Figure S8b). Moreover, the concomitant minor (≤ 5%, Figure S8b) and globally invariant (Figure 10a) contribution of $k_{Nd^*}^{relax} = k_{Nd^*}^{rad} + k_{Nd^*}^{non\text{-}rad}$ to the relaxation mechanism in acetonitrile (Figure 10a) results in the exclusive control of the modulation of the lanthanide emission by the spin-state equilibrium (eq 1), where the strongly quenched LS-$[NdFe(\mathbf{L1})_3]^{5+}$ emitter is replaced stepwise by its more emissive HS-$[NdFe(\mathbf{L1})_3]^{5+}$ counterpart. This transforms the ripple of emission intensity of the steady-state luminescence reported for $[EuFe(\mathbf{L1})_3]^{5+}$ (Figure 1b), which depends on both $k_{Eu^*}^{relax}$ and the SCO

process (Figure 2b),[35] into a straightforward growing curve for [NdFe(**L1**)$_3$]$^{5+}$ (Figure 9b and Figure S9) which corresponds to the direct and quantitative luminescent sensing of the Fe^{II} spin state in [NdFe(**L1**)$_3$]$^{5+}$ (Figure 10b and Figure S10).

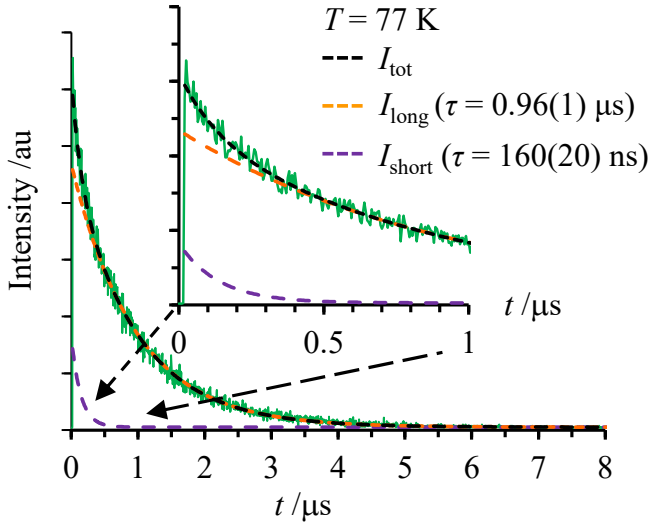

Figure 11. Experimental Nd(^{4}F$_{3/2}$→^{4}I$_{11/2}$) decay curve (green trace) recorded for [NdFe(**L1**)$_3$]$^{5+}$ at $\lambda_{em} \geq 1000$ nm in its frozen acetonitrile solution at 77 K (λ_{exc} = 355 nm, CNI Laser MPL-F-355) highlighting its biexponential fit with eq 4.

Taking [EuFe(**L1**)$_3$]$^{5+}$ as a reference point, the kinetic rate constants controlling the Eu(^{5}D$_0$) visible emission in acetonitrile (Figure 2b) shows that $k_{LS}^{q} \gg k_{HL} \sim k_{LH} \sim k_{Eu^*}^{relax} \geq k_{HS}^{q}$; a situation where the time-dependent europium-based luminescence intensities $I_{Eu^*}(t)$, modeled in eq 4, simplifies to be approached with eq 11 (Appendix 1, $k_A = k_{LH} + k_{Eu^*}^{relax} + k_{LS}^{q} \approx k_{LS}^{q}$ and $k_B = k_{HL} + k_{Eu^*}^{relax} + k_{HS}^{q} \approx k_{HS}^{q}$ are the total decay rate constants of LS-[Eu*Fe(**L1**)$_3$]$^{5+}$, and HS-[Eu*Fe(**L1**)$_3$]$^{5+}$ respectively, which exist as their specific mole fractions x_{LS} and x_{HS} in solution at each temperature).

$$I_{Eu^*}(t) \approx \frac{k_{Eu^*}^{rad}\left(C_1 + D_1\right)}{x_{LS}}\left(x_{LS} \cdot e^{-k_A t} + x_{HS} \cdot e^{-k_B t}\right) \qquad (11)$$

A simple look at the estimated kinetic rate constants controlling the Nd(^{4}F$_{3/2}$) NIR emission luminescence in the dinuclear [NdFe(**L1**)$_3$]$^{5+}$ helicate in acetonitrile (Figure 10a, the associated Arrhenius plots are collected in Figure S1b) shows a different trend with $k_{LS}^{q} > k_{HS}^{q} \sim k_{Nd^*}^{relax} \gg k_{HL}, k_{LH}$

and the simplified eq 11 is only relevant around room temperature. In these specific conditions, the expected double-exponential nature of the normalized intensity $I_{Nd^*}(t)$ reflects the decay rate constants controlling the relaxation of LS-[Nd*Fe(**L1**)$_3$]$^{5+}$ (k_A), respectively HS-[Nd*Fe(**L1**)$_3$]$^{5+}$ (k_B). When considering the rate constants collected in Table 2 for [Nd*Fe(**L1**)$_3$]$^{5+}$ in solution in the 233-333 K range, the associated short characteristic lifetimes $\tau_{short} = 1/k_A \approx 1/k_{LS}^q$ is estimated within tenths of nanoseconds, whereas $\tau_{long} = 1/k_B \approx 1/k_{HS}^q$ reaches the microsecond domain. Such discrimination between a short (very weak) emission arising from LS-[Nd*Fe(**L1**)$_3$]$^{5+}$ and a long 'intense' emission arising from HS-[Nd*Fe(**L1**)$_3$]$^{5+}$) represents a challenge when analyzing the experimental normalized time-resolved intensities of Nd^{III} in [NdFe(**L1**)$_3$]$^{5+}$ (Figure S11a), which can be thus satisfyingly fitted by using a mono-exponential decay within the microsecond range (1.0 to 1.4 μs, Table S2 and Figure S11b). We were not able to safely extract the missing nanosecond information by any satisfying double exponential fit of the experimental decay curves around room temperature (Figure S11a). In frozen acetonitrile at 77K, one expects some significant decrease of the quenching constants k_{LS}^q so that $k_{LS}^q \simeq k_{HS}^q$ (Figure 10 a), and eq 4 is thus only pertinent for a quantitative kinetic analysis. A convincing biexponential decay could be indeed detected for the Nd($^4F_{3/2} \rightarrow {}^4I_{11/2}$) emission collected at wavelength larger than 1000 nm under nanosecond pulsed excitation in these conditions (λ_{exc} = 355 nm, Figure 11). The short lifetime is estimated within the 100 ns range, which is assigned to the emission of Nd(III) in LS-[NdFe(**L1**)$_3$]$^{5+}$ and the long lifetime reaches the microsecond range, which reflects the emission of HS-[NdFe(**L1**)$_3$]$^{5+}$.

Conclusion

The replacement of Ln = Eu^{III} with Nd^{III} in the dinuclear triple-stranded helicate [LnFe(**L1**)$_3$]$^{5+}$ has a very minor effect on the structures and stabilities in both solid state and solution and does not significantly alter the SCO Fe^{II} process, the transition temperature of which reaches 317-322 K in acetonitrile.[35] As planned, the shift of the lanthanide-based emission from the visible (Eu^{III}) to the NIR (Nd^{III}) is accompanied by a considerable increase (3 orders of magnitude) of the non-radiative

quenching rate constants of the emissive state by vibrations ($k_{Ln^*}^{non\text{-}rad}$), which become globally constant for $[NdFe(\mathbf{L1})_3]^{5+}$ in the temperature range accessible in acetonitrile (233-333K, Figure 10a). Unexpectedly enough for the authors, the two intramolecular Förster-based energy transfer processes $Nd^{III}\rightarrow LS\text{-}Fe^{II}$ and $Nd^{III}\rightarrow HS\text{-}Fe^{II}$ are boosted in going from $[EuFe(\mathbf{L1})_3]^{5+}$ to $[NdFe(\mathbf{L1})_3]^{5+}$ due to the combination of (i) larger radiative rate constants, (ii) lower emission energy and (iii) increased spectral overlap. Since $k_{HS}^{q} < k_{LS}^{q}$ is combined with constant $k_{Nd^*}^{relax}$ in the 233-333 K range , the modulation of the $Nd(^4F_{3/2}\rightarrow {}^4I_J)$ NIR emission reflects simply the changes in the appended Fe^{II} spin state equilibrium with an improved sensitivity (Figure 9b). To conclude, the strict correlation between the emission intensity and the mole fraction of high-spin Fe^{II} (Figure 10b) demonstrates the use of Nd^{III} as an ideal sensor for the SCO process and paves the way for the next generation of multifunctional SCO-Fe supramolecular entities, in which abrupt Fe^{II} spin state changes can be locally detected by appended Nd sensors if positive cooperativity could be programmed at the supramolecular level.[13,16,66]

ASSOCIATED CONTENT

Supporting Information

The Supporting Information is available free of charge at https://pubs.acs.org/doi/XXX.
Complete experimental details, complexes syntheses and characterizations, photophysical data and kinetic analysis (PDF).

AUTHOR INFORMATION

Corresponding Author

Claude Piguet - *Department of Inorganic and Analytical Chemistry. University of Geneva, 30 quai E. Ansermet CH-1211 Geneva 4 (Switzerland)*; *orcid.org/0000-0001-7064-8548*
Email: Claude.Piguet@unige.ch

Authors

Neel Deorukhkar - *Department of Inorganic and Analytical Chemistry. University of Geneva, 30 quai E. Ansermet CH-1211 Geneva 4 (Switzerland)*.

Charlotte Egger - *Department of Inorganic and Analytical Chemistry. University of Geneva, 30 quai E. Ansermet CH-1211 Geneva 4 (Switzerland)*.

Arnulf Rosspeintner – *Department of Physical Chemistry, University of Geneva, 30 quai E. Ansermet. CH-1211 Geneva 4 (Switzerland).*

Notes

The authors declare no conflict of interest.

ACKNOWLEGMENTS

This work is supported through grants from the Swiss National Science Foundation (grant 200020_207313).

REFERENCES

(1) McCusker, J. K., Electronic Structure in the Transition Metal Block and Its Implications for Light Harvesting. *Science* **2019**, *363*, 484-488.

(2) Larsen, C. B.; Braun, J. D.; Lozada, I. B.; Kunnus, K.; Biasin, E.; Kolodziej, C.; Burda, C.; Cordones, A. A.; Gaffney, K. J.; Herbert, D. E., Reduction of Electron Repulsion in Highly Covalent Fe-Amido Complexes Counteracts the Impact of a Weak Ligand Field on Excited-State Ordering. *J. Am. Chem. Soc.* **2021**, *143*, 20645-20656.

(3) Friedman Jr., H. G.; Choppin, G. R.; Feuerbacker, D. G., The Shapes of the f Orbitals. *J. Chem. Educ.* **1964**, *41*, 354-358.

(4) Lang, P. F.; Smith, B. C., Ionization Energies of Lanthanides. *J. Chem. Educ.* **2010**, *87*, 875-881.

(5) Gütlich, P.; Goodwin, H. A., Spin Crossover - An Overall Perspective. *Top. Curr. Chem.* **2004**, *233*, 1-47.

(6) Gütlich, P.; Gaspar, A. B.; Garcia, Y. Spin State Switching in Iron Coordination Compounds. *Beilstein J. Org. Chem.* **2013**, *9*, 342–391

(7) Toftlund, H., Spin Equilibria in Iron(II) Complexes. *Coord. Chem. Rev.* **1989**, *94*, 67-108.

(8) Halcrow, M. A., The Spin-States and Spin Transitions of Mononuclear Iron(II) Complexes of Nitrogen-Donor Ligands. *Polyhedron* **2007**, *26*, 3523-3576.

(9) Olguin, J.; Brooker, S., Spin Crossover Active Iron(II) Complexes of Selected Pyrazole-Pyridine/Pyrazine Ligands. *Coord. Chem. Rev.* **2011**, *255*, 203-240.

(10) Hogue, R. W.; Singh, S.; Brooker, S., Spin Crossover in Discrete Polynuclear Iron(II) Complexes. *Chem. Soc. Rev.* **2018**, *47*, 7303-7338.

(11) Sasaki, N.; Kambara, T., Theory of the 2-Step Spin Conversion Induced by the Cooperative Molecular Distortions in Spin-Crossover Compounds. *Phys. Rev. B* **1989**, *40*, 2442-2449.

(12) Bousseksou, A.; Molnar, G.; Salmon, L.; Nicolazzi, W., Molecular Spin Crossover Phenomenon: Recent Achievements and Prospects. *Chem. Soc. Rev.* **2011**, *40*, 3313-3335.

(13) Brooker, S., Spin Crossover with Thermal Hysteresis: Practicalities and Lessons Learnt. *Chem. Soc. Rev.* **2015**, *44*, 2880-2892.

(14) Marciniak, L.; Kniec, K.; Elzbieciak-piecka, K.; Trejgis, K.; Stefanska, J.; Dramicanin, M., Luminescence Thermometry with Transition Metal Ions. A Review. *Coord. Chem. Rev.* **2022**, *469*, 214671.

(15) Shepherd, H. J.; Quintero, C. M.; Molnar, G.; Salmon, L.; Bousseksou, A., Luminescent Spin-Crossover Materials. In Spin-Crossover Materials: Properties and Applications, Halcrow, M. A., Ed, John Wiley & Sons, Ltd, Chichester, **2013**, 13, 347-373.

(16) Kumar, K. S.; Ruben, M., Emerging Trends in Spin Crossover (SCO) Based Functional Materials and Devices. *Coord. Chem. Rev.* **2017**, *346*, 176-205.

(17) Meng, Y. S.; Liu, T., Manipulating Spin Transition To Achieve Switchable Multifunctions. *Acc. Chem. Res.* **2019**, *52*, 1369-1379.

(18) Javed, M. K.; Sulaiman, A.; Yamashita, M.; Li, Z. Y., Shedding Light on Bifunctional Luminescent Spin Crossover Materials. *Coord. Chem. Rev.* **2022**, *467*, 214625.

(19) Salmon, L.; Molnar, G.; Zitouni, D.; Quintero, C.; Bergaud, C.; Micheau, J. C.; Bousseksou, A., A Novel Approach for Fluorescent Thermometry and Thermal Imaging Purposes Using Spin Crossover Nanoparticles. *J. Mater. Chem. C* **2010**, *20*, 5499-5503.

(20) Kraieva, O.; Quintero, C. M.; Suleimanov, I.; Hernandez, E. M.; Lagrange, D.; Salmon, L.; Nicolazzi, W.; Molnar, G.; Bergaud, C.; Bousseksou, A., High Spatial Resolution Imaging of Transient Thermal Events Using Materials with Thermal Memory. *Small* **2016**, *12*, 6325-6331.

(21) Guo, Y.; Xue, S.; Dîrtu, M. M.; Garcia, Y. A Versatile Iron(II)-Based Colorimetric Sensor for the Vapor-Phase Detection of Alcohols and Toxic Gases. J. Mater. Chem. C 2018, 6 (15), 3895–3900. https://doi.org/10.1039/C8TC00375K.

(22) Suleimanov, I.; Kraieva, O.; Sánchez Costa, J.; Fritsky, I. O.; Molnár, G.; Salmon, L.; Bousseksou, A. Electronic Communication between Fluorescent Pyrene Excimers and Spin Crossover Complexes in Nanocomposite Particles. *J. Mater. Chem. C* **2015**, *3*, 5026–5032.

(23) Kraieva, O.; Suleimanov, I.; Molnár, G.; Salmon, L.; Bousseksou, A. CdTe Quantum Dot Fluorescence Modulation by Spin Crossover. *Magnetochemistry* **2016**, *2*, 11.

(24) Wang, J.-L.; Liu, Q.; Meng, Y.-S.; Liu, X.; Zheng, H.; Shi, Q.; Duan, C.-Y.; Liu, T. Fluorescence Modulation via Photoinduced Spin Crossover Switched Energy Transfer from Fluorophores to Fe(II) Ions. *Chem. Sci.* **2018**, *9*, 2892–2897.

(25) Förster, T., 10th Spiers Memorial Lecture - Transfer Mechanisms of Electronic Excitation. *Discuss. Faraday Soc.* **1959**, *27*, 7-17.

(26) Suleimanov, I.; Kraieva, O.; Molnár, G.; Salmon, L.; Bousseksou, A.; Molnar, G.; Salmon, L.; Bousseksou, A. Enhanced Luminescence Stability with a Tb–Spin Crossover Nanocomposite for Spin State Monitoring. *Chem. Commun.* **2015**, *51*, 15098–15101.

(27) Förster, T., Zwischenmolekulare Energiewanderung und Fluoreszenz. *Ann. Phys.* **1948**, *437*, 55-75.

(28) Tanner, P. A.; Zhou, L.; Duan, C.; Wong, K.-L., Misconceptions in Electronic Energy Transfer: Bridging the Gap Between Chemistry and Physics. *Chem. Soc. Rev.* **2018**, *47*, 5234-5265.

(29) Lindsey, J. S.; Taniguchi, M.; Bocian, D. F.; Holten, D., The Fluorescence Quantum Yield Parameter in Förster Resonance Energy Transfer (FRET)-Meaning, Misperception, and Molecular Design. *Chem. Phys. Rev.* **2021**, *2*, 011302.

(30) Birgeneau, R. J.; Hutching, M. T.; Baker, J. M.; Riley, J. D., High-Degree Electrostatic and Exchange Interactions in Rare-Earth Compounds. *J. Appl. Phys.* **1969**, *40*, 1070-1079.

(31) Dexter, D. L., A Theory of Sensitized Luminescence in Solids. *J. Chem. Phys.* **1953**, *21*, 836.

(32) Inokuti, M.; Hirayama, F., Influence of Energy Transfer by the Exchange Mechanism on Donor Luminescence. *J. Chem. Phys.* **1965**, *43*, 1978-1989.

(33) Ito, A.; Meyer, T. J., The Golden Rule. Application for Fun and Profit in Electron Transfer, Energy Transfer, and Excited-State Decay. *Phys. Chem. Chem. Phys.* **2012**, *14*, 13731-13745.

(34) Beltran-Leiva, M. J.; Paez-Hernandez, D.; Arratia-Perez, R., Theoretical Determination of Energy Transfer Processes and Influence of Symmetry in Lanthanide(III) Complexes: Methodological Considerations. *Inorg. Chem.* **2018**, *57*, 5120-5132.

(35) Deorukhkar, N.; Egger, C.; Guenee, L.; Besnard, C.; Piguet, C., Detecting Fe(II) Spin-Crossover by Modulation of Appended Eu(III) Luminescence in a Single Molecule. *J. Am. Chem. Soc.* **2024**, *146*, 308-318.

(36) Eliseeva, S. V; Bünzli, J.-C. G. Lanthanide Luminescence for Functional Materials and Bio-Sciences. *Chem. Soc. Rev.* **2010**, *39*, 189–227.

(37) Bünzli, J.-C. G.; Eliseeva, S. V. Intriguing Aspects of Lanthanide Luminescence. *Chem. Sci.* **2013**, *4*, 1939–1949.

(38) Bünzli, J.-C. G. Lanthanide Luminescence: From a Mystery to Rationalization, Understanding and Applications. In *Handbook on the Physics and Chemistry of Rare Earths*; Bünzli, J.-C. G., Pecharsky, V. K., Eds.; Elsevier Science: Amsterdam, 2016; Vol. 50, pp 141–176.

(39) Bünzli, J.-C. G.; Eliseeva, S. V. Basics of Lanthanide Photophysics. In *lanthanide Luminescence: Photophysical, Anaéytical and Biological Aspects*; Hänninen, P., Härmä, H., Eds.; Springer-Verlag: Berlin, 2010; Vol. 7, pp 1–45.

(40) Lathion, T.; Fürstenberg, A.; Besnard, C.; Hauser, A.; Bousseksou, A.; Piguet, C., Monitoring Fe(II) Spin-State Equilibria via Eu(III) Luminescence in Molecular Complexes: Dream or Reality? *Inorg. Chem.* **2020**, *59*, 1091-1103.

(41) Braslavsky, S. E.; Fron, E.; Rodríguez, H. B.; Román, E. S.; Scholes, G. D.; Schweitzer, G.; Valeur, B.; Wirz, J., Pitfalls and Limitations in the Practical Use of Förster's Theory of Resonance Energy Transfer. *Photoch. Photobio. Sci.* **2008**, *7*, 1444-1448.

(42) Carnall, W. T., The Absorption and Fluorescence Spectra of Rare Earth Ions in Solution. In *Handbook on the Physics and Chemistry of Rare Earths*, Gschneidner, K. A.; Eyring, L., Eds. North-Holland Publishing Company: Amsterdam, New York, Oxford, 1979; Vol. 3, chap 24, pp 171-208.

(43) Bünzli, J.-C. G.; Eliseeva, S. V., Basics of Lanthanide Photophysics. In Lanthanide Luminescence: Photophysical, Analytical and Biological Aspects, Hänninen, P.; Härmä, H., Eds. Springer-Verlag: Berlin Heidelberg, 2010; Vol. 7, pp 1-45.

(44) Nielsen, V. R. M.; Nawrocki, P. R.; Sorensen, T. J., Electronic Structure of Neodymium(III) and Europium(III) Resolved in Solution Using High-Resolution Optical Spectroscopy and Population Analysis. *J. Phys. Chem. A* **2023**, *127*, 3577-3590.

(45) Hauser, A., Ligand Field Theoretical Considerations. *Top. Curr. Chem.* **2004**, *233*, 49-58.

(46) Billard, I., Lanthanide and Actinide Solution Chemistry Studied by Time-Resolved Emission Spectroscopy. In *Handbook on the Physics and Chemistry of Rare Earths*, Gschneidner Jr, K. A.; Bünzli, J.-C. G.; Pecharsky, V. K., Eds. Elsevier Science: Amsterdam, 2003; Vol. 33, pp 465-514.

(47) Dossing, A., Luminescence from Lanthanide(3+) Ions in Solution. *Eur. J. Inorg. Chem.* **2005**, 1425-1434.

(48) Nawrocki, P. R.; Sorensen, T. J., Optical Spectroscopy as a Tool for Studying the Solution Chemistry of Neodymium(III). *Phys. Chem. Chem. Phys.* **2023**, *25*, 19300-19336.

(49) Wang, Z. M.; Xing, B. G., Near-Infrared Multipurpose Lanthanide-Imaging Nanoprobes. *Chem. Asian. J.* **2020**, *15*, 2076-2091.

(50) Piguet, C.; Geraldes, C. F. G. C., Paramagnetic NMR lanthanide induced shifts for extracting solution structures. In *Handbook on the Physics and Chemistry of Rare Earths*, Gschneidner Jr, K. A.; Bünzli, J.-C. G.; Pecharsky, V. K., Eds. Elsevier Science: Amsterdam, 2003; Vol. 33, pp 353-463.

(51) Peters, J. A.; Djanashvili, K.; Geraldes, C. F. C. G.; Platas-Iglesias, C., The Chemical Consequences of the Gradual Decrease of the Ionic Radius Along the Ln-Series. *Coord. Chem. Rev.* **2020**, *406*, 213146.

(52) Strickler, S. J.; Berg, R. A., Relationship between Absorption Intensity and Fluorescence Lifetime of Molecules. *J. Chem. Phys.* **1962**, *37*, 814-822.

(53) Werts, M. H. V.; Jukes, R. T. F.; Verhoeven, J. W. The Emission Spectrum and the Radiative Lifetime of Eu^{3+} in Luminescent Lanthanide Complexes. *Phys. Chem. Chem. Phys.* **2002**, *4*, 1542–1548.

(54) Bünzli, J.-C. G.; Chauvin, A.-S.; Kim, H. K.; Deiters, E.; Eliseeva, S. V., Lanthanide Luminescence Efficiency in Eight- and Nine-Coordinate Complexes: Role of the Radiative Lifetime. *Coord. Chem. Rev.* **2010**, *254*, 2623-2633.

(55) Sardar, D. K.; Chandrasekharan, S.; Nash, K. L.; Gruber, J. B., Optical Intensity Analyses of Er^{3+}:$YAlO_3$. *J. Appl. Phys.* **2008**, *104*, 023102.

(56) Ajith Kumar, G.; Biju, P. R.; Venugopal, C.; Unnikrishnan, N. V. Spectroscopic Parameters of Nd^{3+} Ion in Phosphate Glasses. *J. Non. Cryst. Solids* **1997**, *221*, 47–58.

(57) Trautnitz, M. F. K.; Doffek, C.; Seitz, M. Radiative Lifetime, Non-Radiative Relaxation, and Sensitization Efficiency in Luminescent Europium and Neodymium Cryptates – The Roles of 2,2′-Bipyridine- N,N′ -dioxide and Deuteration. *ChemPhysChem* **2019**, *20*, 2179–2186.

(58) Shavaleev, N. M.; Scopelliti, R.; Gumy, F.; Bünzli, J.-C. G. J.-C. G. Modulating the Near-Infrared Luminescence of Neodymium and Ytterbium Complexes with Tridentate Ligands Based on Benzoxazole-Substituted 8-Hydroxyquinolines. *Inorg. Chem.* **2009**, *48*, 2908–2918.

(59) Hilborn, R. C., Einstein Coefficients, Cross-Sections, *F* Values, Dipole-Moments, and All That. *Am. J. Phys.* **1982**, *50*, 982-986.

(60) Brik, M. G., Ma, C.-G., *Theoretical Spectroscopy of Transition Metal and Earth Ions: From free State to Crystal Field,* Jenny Stanford Publishing Pte. Ltd., 2020, pp 213-215 and 222-224.

(61) Marciniak, L.; Kniec, K.; Elzbieciak-Piecka, K.; Trejgis, K.; Stefanska, J.; Dramicanin, M., Luminescence Thermometry with Transition Metal Ions. A Review. *Coord. Chem. Rev.* **2022**, *469*, 214671.

(62) Reinhard, C.; Güdel, H. U., High-Resolution Optical Spectroscopy of $Na_3[Ln(dpa)_3]\cdot 13H2O$ with Ln = Er, Tm, Yb. *Inorg. Chem.* **2002**, *41*, 1048-1055.

(63) Henderson, B.; Imbush, G. F., *Optical Spectroscopy of Inorganic Solids* in Monographs on the Physics and Chemistry of Materials, 44, chaps 4-9, Oxford University Press, Oxford, 2006.

(64) Shavaleev, N. M.; Scopelliti, R.; Gumy, F.; Bünzli, J.-C. G. J.-C. G. Near-Infrared Luminescence of Nine-Coordinate Neodymium Complexes with Benzimidazole-Substituted 8-Hydroxyquinolines. *Inorg. Chem.* **2008**, *47*, 9055–9068.

(65) Yanagida, S.; Hasegawa, Y.; Murakoshi, K.; Wada, Y.; Nakashima, N.; Yamanaka, T. Strategies for Enhancing Photoluminescence of Nd3+ in Liquid Media. *Coord. Chem. Rev.* **1998**, *171*, 461–480.

(66) Telfer, S. G.; Bocquet, B.; Williams, A. F., Thermal Spin Crossover in Binuclear Iron(II) Helicates: Negative Cooperativity and a Mixed Spin State in Solution. *Inorg. Chem.* **2001**, *40*, 4818-4820.

TOC Graphic

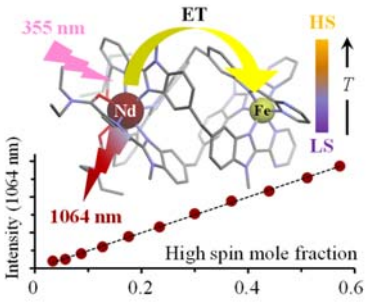
355 nm
ET
HS
T
LS
Nd
Fe
1064 nm
Intensity (1064 nm)
High spin mole fraction
0
0.2
0.4
0.6